ARTICLE

Ultra-Low-Power E-Nose System Based on Multi-Micro-LED-Integrated, Nanostructured Gas Sensors and Deep Learning

Kichul Lee, Incheol Cho, Mingu Kang, Jaeseok Jeong, Minho Choi, Kie Young Woo, Kuk-Jin Yoon,* Yong-Hoon Cho,* and Inkyu Park*

Read Online

ACCESS | Metrics & More | Article Recommendations | SI Supporting Information

ABSTRACT: As interests in air quality monitoring related to environmental pollution and industrial safety increase, demands for gas sensors are rapidly increasing. Among various gas sensor types, the semiconductor metal oxide (SMO)-type sensor has advantages of high sensitivity, low cost, mass production, and small size but suffers from poor selectivity. To solve this problem, electronic nose (e-nose) systems using a gas sensor array and pattern recognition are widely used. However, as the number of sensors in the e-nose system increases, total power consumption also increases. In this study, an ultra-low-power e-nose system was developed using ultraviolet (UV) micro-LED (μLED) gas sensors and a convolutional neural network (CNN). A monolithic photoactivated gas sensor was developed by depositing a nanocolumnar In_2O_3 film coated with plasmonic metal nanoparticles (NPs) directly on the μLED. The e-nose system consists of two different μLED sensors with silver and gold NP coating, and the total power consumption was measured as 0.38 mW, which is one-hundredth of the conventional heater-based e-nose system. Responses to various target gases measured by multi-μLED gas sensors were analyzed by pattern recognition and used as the training data for the CNN algorithm. As a result, a real-time, highly selective e-nose system with a gas classification accuracy of 99.32% and a gas concentration regression error (mean absolute) of 13.82% for five different gases (air, ethanol, NO_2, acetone, methanol) was developed. The μLED-based e-nose system can be stably battery-driven for a long period and is expected to be widely used in environmental internet of things (IoT) applications.

KEYWORDS: micro-LED, monolithic photoactivated gas sensor, ultra-low-power, localized surface plasmon resonance, deep learning algorithm, electronic nose
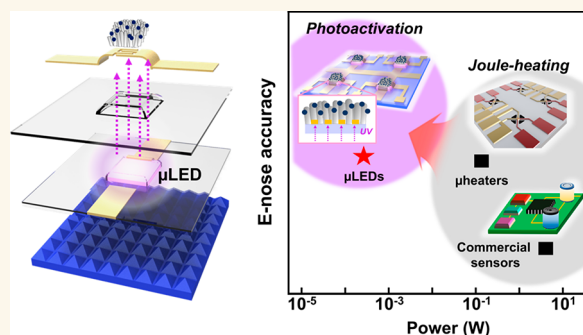
INTRODUCTION

Air pollution has become one of the biggest problems that modern society faces, and environmental safety and ESG (environmental, social, governance) have become mainstream in global society.[1] Owing to worldwide interest in environmental problems and smart healthcare, the need for gas sensors that can systematically monitor the environment has rapidly increased. Traditionally, gas sensors have been mainly used in monitoring air pollutants and toxic gases occurring in industrial, livestock, and agricultural facilities.[2-4] Recently, their application has become wider such as home indoor air quality monitoring, early diagnosis of diseases through exhalation analysis, and food spoilage monitoring.[5-7] The gas sensors are classified according to their gas detection principles, and there are electrochemical, catalytic combustion, nondispersive infrared (NDIR), and semiconductor metal

oxide (SMO)-type gas sensors.[8-13] Among them, the SMO-type gas sensors are being studied most actively owing to their high sensitivity, compact size, low price, and mass producibility.[13] SMO-type gas sensors detect the target gas by the change in the electrical resistance of the metal oxide when exposed to the target gas. SMO-type gas sensors require activation for higher sensitivity and faster response and recovery speeds. When the metal oxide is energetically activated, hot electron—hole pairs are generated, which act as
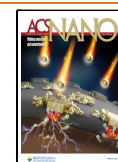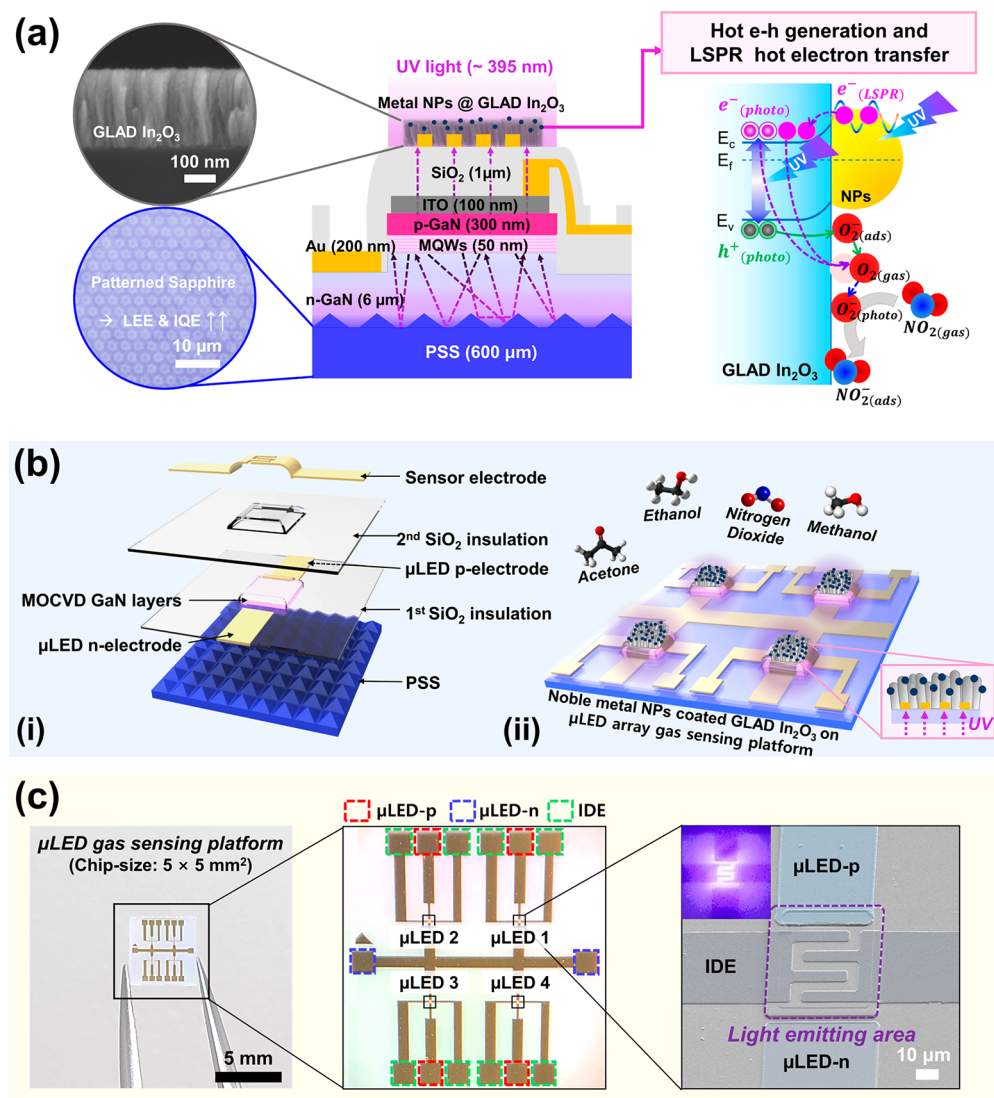
Figure 1. (a) Schematic images of structure and sensing mechanism of the UV μLED gas sensor. Extremely small distance (the thickness of the SiO_2 insulation layer is approximately 1 μm) between the light source and the gas sensing material minimizes the energy loss and enables ultra-low-power gas detection. Noble metal NPs were coated on the surface of the nanocolumnar GLAD In_2O_3 and gas response was improved by LSPR. (b) 3D illustration images of (i) the laminated structure of the μLED gas sensing platform and (ii) GLAD In_2O_3 coated with noble metal NPs deposited on the μLED array platform. (c) Fabrication results of μLED gas sensing platform. After wafer-scale fabrication, substrate was diced into single sensor chips of 5 × 5 mm^2.

carriers and promote the redox reaction of the target gas.[13] In general, a joule heating method (250−400 °C) with a built-in heater has been widely used, but it consumes high power and there is a possibility of igniting explosive gas such as hydrogen. To minimize the power consumption, microfabricated micro-heaters[14,15] and self-heating nanowires[16,17] were developed, but their suspended structures are vulnerable to mechanical and thermal stresses, and their fabrication processes are complicated and expensive. On the other hand, chemical sensing by photoactivation is attracting attention because it can be operated at room temperature (RT) and can operate safely in any environmental conditions.[18−20] However, most of the previous studies used external lamps or commercial LEDs as light sources, so power consumption was large on a few watt scale. In our previous work, we developed a monolithic photoactivated gas sensor using an ultraviolet (UV) micro-LED (μLED) as a light source.[21] Gas-sensitive ZnO nanowires were hydrothermally grown directly on the μLED platform,

and optical loss reduction enabled gas detection with an ultra-low-power consumption of 184 μW. Meanwhile, SMO-type gas sensors have a nonselective resistance change to various target gases.[13,22] Many attempts have been made to solve this nonselectivity problem, and electronic nose (e-nose) systems that mimic and advance human olfaction are considered as the most promising method. The e-nose system consists of multiple gas sensor arrays that each exhibit different responses to specific target gases and a learning algorithm that conducts a pattern recognition algorithm of the sensor signals.[23−26] As the number of sensors used in the e-nose systems increases, it becomes more important to reduce the power and volume of individual sensors.

In this study, an ultra-low-power e-nose system based on multi-UV-μLED gas sensors was developed. A porous, nanocolumnar In_2O_3 film was deposited directly on the μLEDs through glancing angle deposition (GLAD) and used as a gas sensing material. In order to increase the gas response

of the sensors, the localized surface plasmon resonance (LSPR) phenomenon was utilized by coating plasmonic metal nanoparticles (NPs) on the surface of the metal oxide nanostructures by e-beam evaporation. The responses to various target gases were simultaneously measured by two different μLED sensors coated with silver (Ag) and gold (Au) NPs, respectively, and unique transient sensor signals made by specific gases were captured by a sliding time window during data preprocessing. Finally, preprocessed data were used as the training data for a convolutional neural network (CNN) algorithm, and as a result, a highly accurate e-nose system that can selectively predict five gases (air, ethanol, NO_2, acetone, and methanol) in real-time was developed. The e-nose system developed in this study is composed of monolithic photo-activated gas sensors, and it can be operated at RT with a low power consumption of less than 0.4 mW, showing the possibility of a future mobile gas sensor.

RESULTS AND DISCUSSION

Fabrication of Monolithic Photoactivated UV μLED Gas Sensor. In Figure 1a, a schematic of the μLED gas sensor and its gas sensing mechanism are described. The monolithic photoactivated gas sensor was developed after insulating the μLEDs with plasma-enhanced chemical vapor deposition (PECVD) SiO_2 and patterning the interdigitated sensor electrode (IDE). An epitaxial gallium nitride (GaN) grown sapphire wafer which emits 395 nm wavelength UV light was used for lateral μLED fabrication. The entire microelectro-mechanical system (MEMS) fabrication process was conducted at a wafer-scale, and the detailed fabrication process is described in the Methods section (Figure S1, Supporting Information). In our previous study, the sensor electrode and the p and n electrodes of the μLEDs were on the same plane, and it was necessary to define the sensing area where sensing material is deposited; otherwise, there was a possibility of electrical short.[21] In this study, the sensor structure was modified and a double SiO_2 insulation layer was used to avoid electrical short between the sensor electrode and the p, n electrodes of the μLEDs. Therefore, any gas sensing materials (SMOs, metal–organic frameworks, MXenes, etc.) and their deposition methods can be used. The difference between the previous study using a single SiO_2 layer and this study using a double SiO_2 layer is shown in more detail in Figure S2 (Supporting Information). In addition, the light extraction efficiency (LEE) and internal quantum efficiency (IQE) of the μLEDs were improved by a patterned sapphire substrate (PSS). The PSS technology reduces the dislocation density between the sapphire and GaN layers and increases the IQE and LEE of the μLEDs. The PSS technique also reduces total internal reflection at the interface between air and GaN, allowing more light to be extracted to the upper surface where the SMO sensor is located.[27] Various sizes of μLEDs (30 × 30, 50 × 50, and 100 × 100 μm²) were fabricated and their light–current–voltage (L-I-V) characteristics were analyzed (Figure S3, Supporting Information). The peak wavelength of the emitted light of the fabricated μLEDs was 395 nm, and the full width at half-maximum was 14 nm. In this study, a μLED with a size of 50 × 50 μm² was chosen because it has the highest external quantum efficiency (EQE) and is large enough to reliably deposit gas sensing materials. After fabrication of the μLED gas sensing platform, a porous nanocolumnar In_2O_3 film was deposited directly on the μLED via a wafer-scale glancing angle deposition (GLAD) process. GLAD is a type of RF

sputtering in which physical vapor deposition (PVD) of a target material is performed while the substrate is tilted (Figure S4, Supporting Information).[28,29] During GLAD, a nanoscale self-shadowing effect occurs and a porous columnar nano-structure is formed as a consequence. It has the advantages of high-throughput, large surface-to-volume ratios, high sensor-to-sensor uniformity, and easy processing.[30] In_2O_3 was chosen as a gas sensing material because it is a representative photocatalytic metal oxide suitable for overcoming the bandgap energy (E_g) by UV light and has excellent crystallinity without an additional annealing process after GLAD. A 1 μm thick SiO_2 layer was used for the insulating layer between the sensing material and the μLEDs, which minimizes light energy loss and enables ultra-low-power gas detection. To maximize the performance of the photoactivated gas sensor, plasmonic noble metal NPs were coated on the GLAD In_2O_3 surface by e-beam evaporation. The right side of Figure 1a illustrates the NO_2 gas sensing mechanism of NP-coated GLAD In_2O_3 under μLED illumination. First, in dark conditions, oxygen molecules in the air are adsorbed on the surface of metal oxides mainly in the form of chemisorbed oxygen ions ($O_{2(gas)} + e^- \rightarrow O_2^-_{(ads)}$). When light with a wavelength of 250 to 450 nm is irradiated, hot electron−hole pairs, $e^-_{(photo)}$−$h^+_{(photo)}$ are photogenerated, and the carrier density and electrical conductivity become much higher than in the dark state.[31] The photogenerated holes, $h^+_{(photo)}$ and the chemisorbed oxygen ions, $O_2^-_{(ads)}$ interact and desorb oxygen ions from the surface in the form of $h^+_{(photo)} + O_2^-_{(ads)} \rightarrow O_{2(gas)}$. The desorbed $O_{2(gas)}$ and pre-existing $O_{2(gas)}$ react with photogenerated electrons and form photoadsorbed oxygen ($O_{2(gas)} + e^-_{(photo)} \rightarrow O_2^-_{(photo)}$). The photoadsorbed $O_2^-_{(photo)}$ is weakly bound to the SMO surface and more reactive than chemisorbed oxygen ions, $O_2^-_{(ads)}$.[32] The adsorption and desorption of oxygen molecules on the surface of the SMO gradually reaches an equilibrium state.[31] As the oxidizing gas such as NO_2 approaches the SMO surface, it steals electrons from the photoadsorbed oxygen of the SMO as $NO_{2(gas)} + O_2^-_{(photo)} \rightarrow NO_2^-_{(ads)} + O_{2(gas)}$ or directly traps electrons in the conduction band of metal oxide as $NO_2 + e^- \rightarrow NO_2^-_{(ads)}$. Since the In_2O_3 is an n-type semiconductor, the concentration of carriers decreases, and the electrical resistance increases.[13] As mentioned above, light illumination increases the response because the photogenerated electron−hole pair desorbs chemisorbed $O_2^-_{(ads)}$ and secures a reaction site with the target gas on the SMO surface. Also, adsorption of $NO_{2(gas)}$ and desorption of $O_{2(gas)}$ are accelerated by the photo-generated electron−hole pair, so that the response and recovery speeds of the chemical reaction become faster.[18,32] Additionally, a localized surface plasmon resonance (LSPR) phenomenon occurs when the light is illuminated on the plasmonic NPs that are significantly smaller than the wavelength of the incident light.[33−36] The LSPR results in a strong electric field and a high concentration of energetic electrons near the NPs due to the oscillation and Coulombic restoring force caused by the redistribution of the charge density of the NPs. Following the dynamics of the LSPR, size of the NPs, and radiance of the plasmon, the oscillation of electrons decays through two competitive pathways, radiative and nonradiative decays.[34,36] The nonradiative decay process generates hot electrons of a high energy state, and they can be transferred from NPs to the contacting SMO. Therefore, functionalization of the SMO by the NP coating produces an extra carrier for the SMO and contributes to (1) higher response and (2) faster response and recovery.[32] Details of the
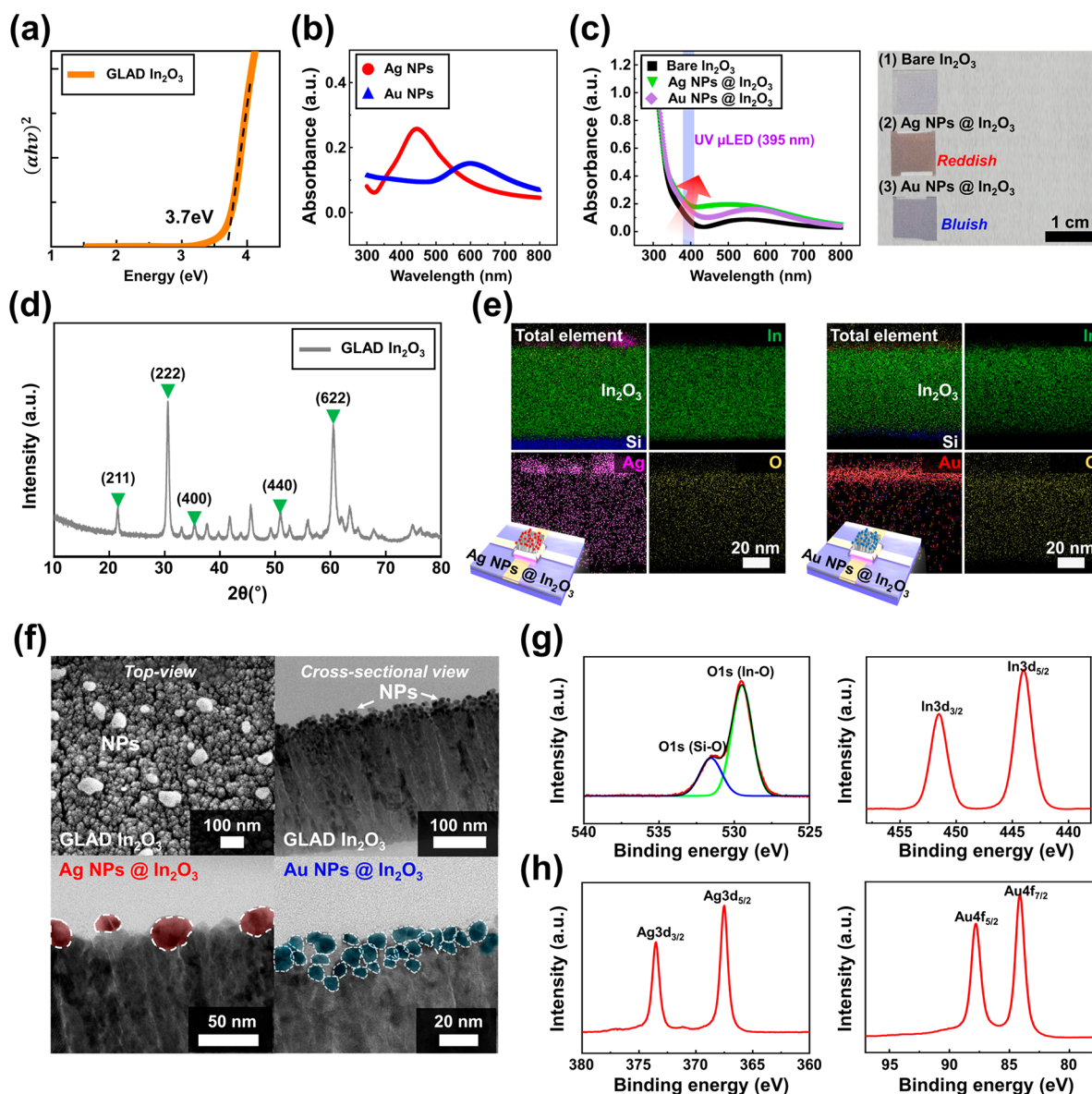
Figure 2. (a) Tauc plot of GLAD In_2O_3 and (b, c) UV−vis spectroscopy of (b) Ag and Au NPs and (c) GLAD In_2O_3 coated with Ag and Au NPs. (d) XRD results of GLAD In_2O_3. No additional annealing was required. (e) EDS mapping results of Ag NP coated In_2O_3 and Au NP coated In_2O_3. (f) SEM (top view) and TEM (cross-sectional view) images of metal NP coated In_2O_3. XPS spectra of (g) O 1s and In 3d and (f) Ag 3d and Au 4f of GLAD In_2O_3 coated with each metal NP (Ag, Au).

NP-functionalized GLAD In_2O_3 are discussed in a later section. Figure 1b shows the 3D illustration images of the laminated structure of the μLED gas sensor and a sensor chip. Four μLEDs exist in a 2 × 2 array on a single sensor chip, and UV light emitted from the bottom is transmitted to the gas sensing material. Meanwhile, the bottom illumination of the SMO has an advantage for gas detection. Since the root of the GLAD In_2O_3 has the shortest distance from the μLED, the concentration of photogenerated electrons is the highest. Electrons can flow directly between the nanocolumns through the bottom surface, shortening the migration path. Therefore, under bottom-illumination, gas-sensing materials can have low resistance and fast response and recovery.[37] Figure 1c shows the fabrication results of the μLED gas sensor. The size of the sensor chip is 5 × 5 mm^2, and the light-emitting area is 50 × 50 $μm^2$. The red, blue, and green dotted areas represent the μLED-p, μLED-n, and sensor electrode pads, respectively, and

the rest of the areas are insulated with the PECVD SiO_2 layer. The right side of Figure 1c is a scanning electron microscope (SEM) image of a 50 × 50 $μm^2$ sized μLED gas sensor, and the inset image shows a UV-emitting μLED at 3.0 V forward bias.

Characterization of NP Functionalized GLAD In_2O_3 Gas Sensing Material. After the GLAD process for the μLED gas sensor, the structure of the nanocolumnar In_2O_3 was analyzed by ultra-high-resolution scanning electron microscopy (UHR-SEM, SU8230, Hitachi, Japan). The thickness of the nanocolumns was 250 nm (Figure 1a) and the porosity (top-view area of voids/total top-view area) was 34.6% (Figure S5, Supporting Information). The porous nanostructure formed by GLAD increases the surface-to-volume ratio and improves reactivity with the target gas. After that, plasmonic noble metal NPs were coated on the GLAD In_2O_3 surface by e-beam evaporation. In this study, Ag and Au, which are representative plasmonic metals, were used, and optimal coating conditions
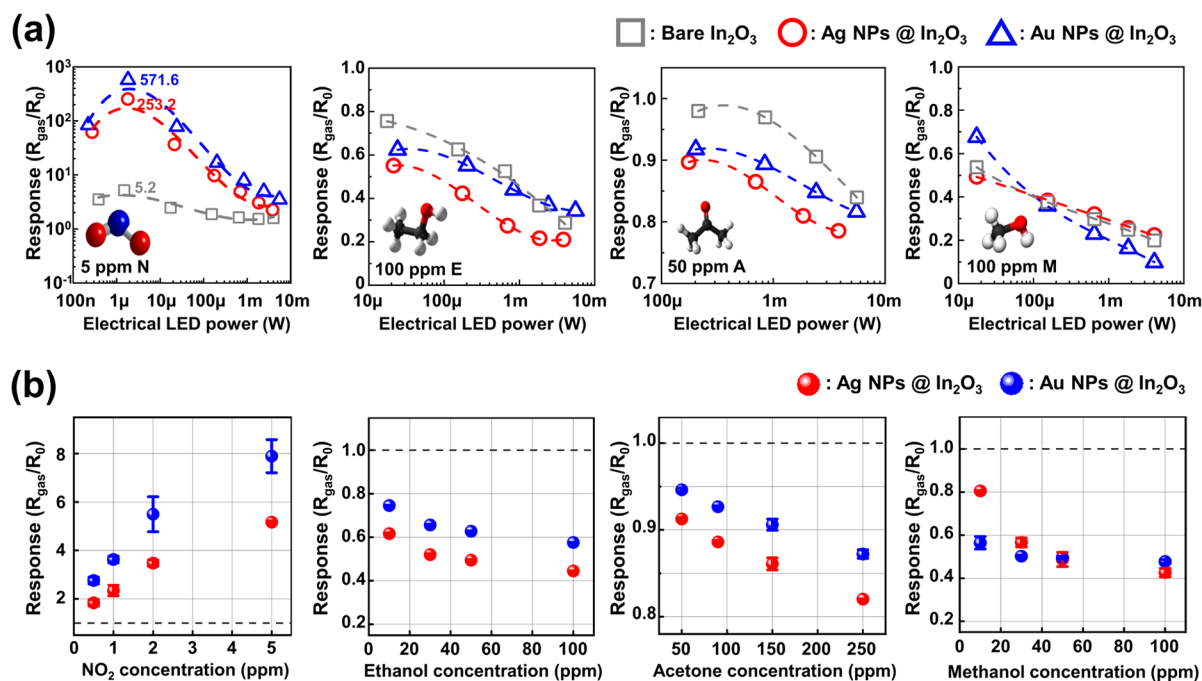
Figure 3. Gas sensing performance of UV μLED gas sensors. (a) Gas responses at various μLED powers for 5 ppm NO_2 (N), 100 ppm ethanol (E), 50 ppm acetone (A), and 100 ppm methanol (M). (b) Gas responses to various concentrations of each target gas. The operation powers of sensors 1 (GLAD In_2O_3 coated with Ag NPs) and 2 (GLAD In_2O_3 coated with Au NPs) were 0.18 mW and 0.20 mW, respectively.

were studied in preliminary experiments before being applied to the actual μLED gas sensors. First, the sizes of NPs according to the e-beam evaporation conditions were examined. Based on the quartz crystal microbalance (QCM) sensor of the e-beam evaporator, Ag and Au NPs were coated on a bare silicon substrate with deposition thicknesses of 1.5, 2.0, and 2.5 nm. The thicker the e-beam deposition thickness, the larger the average size of the NPs became. According to the literature, the LSPR phenomenon predominantly occurs when the size of the plasmonic metal NPs is similar to or smaller than their electron mean free path.[34] The electron mean free paths of Ag and Au are 53.3 and 37.7 nm, respectively.[38] Even under the condition of 2.5 nm thick coating, the average sizes of Ag and Au NPs were smaller than those electron mean free paths, and the LSPR phenomenon could be utilized (Figure S6, Supporting Information). Next, a pilot gas test was performed to confirm the actual effect of the noble metal NP coating on the gas response enhancement. The materials were prepared on top of an interdigitated sensor electrode patterned on a transparent quartz substrate and a commercial UV chip-LED (SM0603UV-390, Bivar, USA) was used as the light source. The recipe for GLAD sputtering of In_2O_3 and e-beam coating of NPs was the same as before. The peak wavelength of the UV chip-LED was 390 nm, and the operation power was 160 mW. NO_2 gas test was conducted by GLAD In_2O_3 coated with metal NPs of various thicknesses, and the response to 7 ppm NO_2 gas was compared (Figure S7, Supporting Information). Bare In_2O_3 without metal NP coating showed a gas response of 21.5 (R_{gas}/R_0, R_{gas} is final value of sensor resistance changed by the target gas, R_0 is the base resistance in air). In the case of the Au NPs, the 2.0 nm thick coating showed the highest response of 4114.4, and in the case of the Ag NPs, the 2.5 nm thick coating showed the highest response of 1868.5. The gas response of In_2O_3 coated with Au and Ag NPs was increased by 191.4 and 86.9 times, respectively,

compared to bare In_2O_3. On the other hand, In_2O_3 coated with 1.5 nm thick nonplasmonic platinum NPs showed a gas response of 9.1, which was lower than that of bare In_2O_3. Therefore, it can be concluded that the LSPR caused by the plasmonic metal NP coating on the GLAD In_2O_3 surface dramatically improved the gas response. A 2.5 nm thick Ag NP coating and a 2.0 nm thick Au NP coating, which showed the highest gas response in the pilot gas test, were applied to the actual UV μLED gas sensor. As a result, μLED gas sensors with different sensing materials were fabricated (sensor 1, GLAD In_2O_3 coated with Ag NPs; sensor 2, GLAD In_2O_3 coated with Au NPs).

Furthermore, utilization of LSPR through plasmonic metal NP coating on metal oxide shifts the light absorbance wavelength of the sensing material, and as a result, the photoactivation efficiency by UV light can be improved. The light absorbance spectra of GLAD In_2O_3, Ag and Au NPs, and GLAD In_2O_3 coated with Ag and Au NPs were measured. In Figure 2a, the Tauc plot of GLAD In_2O_3 is shown after ultraviolet−visible (UV−vis) absorbance spectra measurement of GLAD In_2O_3, and its bandgap was approximately 3.7 eV. The bandgap energy of GLAD In_2O_3 corresponds to the light energy below a wavelength of 335 nm, and there is a mismatch with UV light emitted by the μLED. Figure 2b,c shows the UV−vis spectroscopy results of 2.5 nm thick Ag NPs and 2.0 nm thick Au NPs, and metal NP coated GLAD In_2O_3, respectively. Ag NPs mainly absorbed blue light (550−650 nm) and 2.0 nm thick Au NPs absorbed red light (400−500 nm), which are longer than the UV light wavelength. In Figure 2c, by applying the metal NP coating on the metal oxide surface, light absorption of GLAD In_2O_3 in the visible light was enhanced. The absorbance of GLAD In_2O_3 in the 395 nm wavelength light was increased by 2.22-fold and 1.89-fold by the Ag NP coating and the Au NP coatings, respectively. Ag and Au NP coating on the metal oxide actually made the
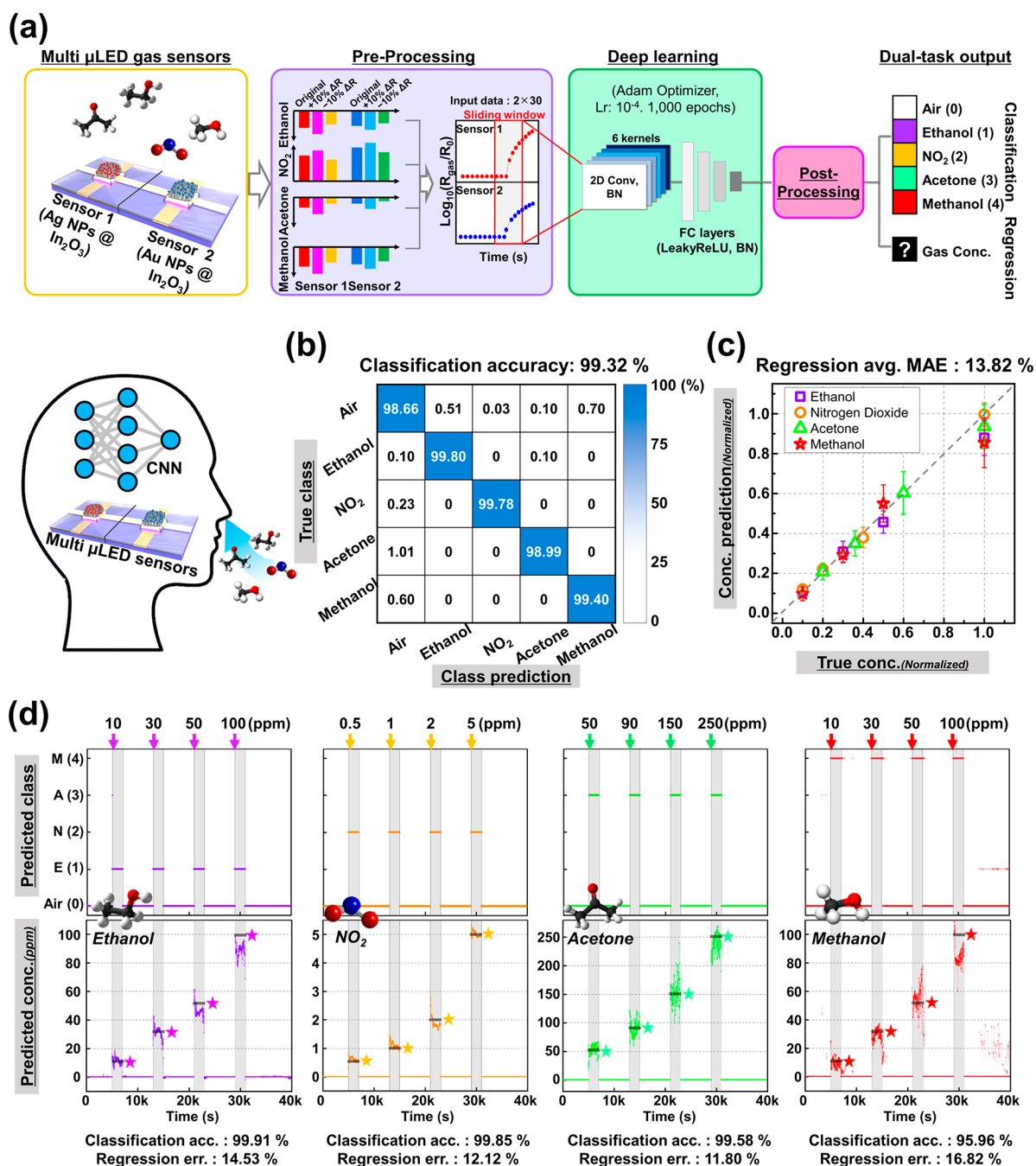
Figure 4. (a) Structure of e-nose system based on multi-μLED gas sensors and CNN algorithm for selectively classifying five gases (air, ethanol, NO$_2$, acetone, and methanol) and quantifying concentrations of each gas. (b) Gas type classification results are summarized in the confusion matrix, and (c) regression results of gas concentration are normalized from 0 to 1. (d) Real-time prediction results of each target gas.

GLAD In$_2$O$_3$ appear reddish and bluish. Therefore, in photoactivated gas sensors, a plasmonic metal NP coating on a base gas sensing material can improve the gas response by enriching hot electrons and controlling the absorbance spectrum through LSPR. In Figure 2d, the GLAD sputtered In$_2$O$_3$ film showed accurate X-ray diffraction (XRD) peaks of In$_2$O$_3$, and no additional annealing process was required after sputtering. Energy dispersive spectrum (EDS) mapping shows that Ag NPs and Au NPs are well coated on the GLAD In$_2$O$_3$ (Figure 2e). The morphology of the metal NP coated GLAD In$_2$O$_3$ nanostructure was analyzed by SEM and transmission electron microscopy (TEM) (Figure 2f). The average

diameters of Ag and Au NPs coated on GLAD In$_2$O$_3$ in the TEM image were 31 and 10 nm, respectively. The XPS spectra of O 1s and In 3d peaks of GLAD In$_2$O$_3$ coated with metal NPs are shown in Figure 2g, and XPS spectra of Ag (3d) and Au (4f) NPs are shown in Figure 2h. This indicates that there was no change in chemical composition of each metal NP and In$_2$O$_3$ during the e-beam evaporation process.

Evaluation of UV μLED Gas Sensor. First, gas response to the μLED power was analyzed to find the optimal operating power of the μLEDs. Figure 3a shows the gas response (R_{gas}/R_0) of bare In$_2$O$_3$, Ag NP coated In$_2$O$_3$, and Au NP coated In$_2$O$_3$ at different μLED electrical powers to 5 ppm NO$_2$ (N),

100 ppm ethanol (E), 50 ppm acetone (A), and 100 ppm methanol (M). The real-time sensor signal for each target gas at different μLED power operations is shown in Figures S8, S9, S10, and S11 (Supporting Information). Since NO_2 is an oxidizing gas, it attracts electrons from the In_2O_3 surface, reducing the conductivity of In_2O_3.[13] Reducing VOC gases, such as ethanol, acetone, and methanol, react with oxygen ions on the surface of In_2O_3 and give up electrons and increase the electrical conductivity. The trend of gas response to μLED power was different for oxidizing and reducing gases. For NO_2 gas, the response was maximal at mid-light-intensity around 1 μW, and for VOC gases, as the power of the μLED increased, the response also increased monotonically (Figure 3a). In general, as the light intensity increases, the desorption of oxygen ions preadsorbed on the surface of the metal oxide is promoted and more hot electrons are generated, thereby increasing the sensor response. However, when the power of the μLED was greater than 1 μW, the gas response to NO_2 decreased and showed a bell-shaped response tendency. According to Prades *et al.*, oxidizing gases such as NO_2 and ozone compete with oxygen for the same adsorption sites on the metal oxide surface and cannot be adsorbed under excessive photon flux, resulting in poor gas response.[39] Therefore, when sensing oxidizing gas, it is important to find the optimal light intensity for lower power consumption and high gas response. On the other hand, reducing VOC gases require chemisorbed oxygen ions to interact with the metal oxide surface and do not compete for the same adsorption site. However, Alenezi reported the same bell-shaped tendency for reducing VOC gases (ethanol, acetone, toluene, and isopropanol) using ZnO nanostructures and a UV lamp (365 nm wavelength).[40] According to the research, the response of VOC gas decreases at high light illumination because hot electrons on the metal oxide surface form stronger hydrogen bonds between VOC gas molecules and surface oxygen. It prevents VOC gases from escaping from the metal oxide surface and lowers the available surface area for detecting subsequent incoming gases. Meanwhile, UV light is effective for hot electron generation and adsorption/desorption reaction of gas molecules but is not sufficient for overcoming the water molecule formation energy that is generated during the chemical reaction with reducing VOC gas.[18,41] It means that stronger light intensity is required to detect VOC gas than oxidizing gas, and so was the experimental result of this study. If the μLED power was higher than the value shown in Figure 3a, the bell-shaped tendency of gas response would have been identified for the VOC gas as well. The effect of metal NP coating on GLAD In_2O_3 on improving the gas response was also confirmed. The gas responses to 5 ppm NO_2 gas at 1 μW power range were 5.2, 253.2, and 571.6 (R_{gas}/R_0) for bare In_2O_3, Ag NP coated In_2O_3, and Au NP coated In_2O_3, respectively. The metal NP functionalization of GLAD In_2O_3 increased the response by more than 100 times compared to the bare GLAD In_2O_3. For VOC gases, the NP coated sensor generally showed higher response, too. Therefore, GLAD In_2O_3 coated with Ag and Au NPs was used for development of a photoactivated e-nose system. The optimal operation condition of μLEDs, which can detect both oxidizing and reducing target gases, was when the forward bias was 3.0 V. In this condition, the power consumptions of sensor 1 (GLAD In_2O_3 coated with Ag NPs) and sensor 2 (GLAD In_2O_3 coated with Au NPs) were 0.18 mW and 0.20 mW, respectively, which means the total power of the e-nose system is only 0.38 mW.

Figure 3b shows the gas test results with various concentrations under the aforementioned conditions (NO_2: 0.5, 1, 2, 5 ppm; ethanol: 10, 30, 50, 100 ppm; acetone: 50, 90, 150, 250 ppm; methanol: 10, 30, 50, 100 ppm). Each gas experiment was repeated twice under the same conditions, and the standard deviation and mean of the response values are shown in the graph. Especially, ethanol and methanol gases were tested at the same concentrations, and it is difficult to selectively distinguish each gas because the magnitude of the gas reaction is also similar. To solve this low selectivity problem, gas sensor data collected by multi-μLED gas sensors were applied to a deep learning algorithm. Real-time sensor signals for various concentrations of each gas are shown in Figure S12 (Supporting Information).

Selective E-Nose System Based on Multi-μLED Gas Sensors and Deep Learning. Figure 4a describes the structure of an e-nose system based on multi-μLED gas sensors and a deep learning algorithm. Until now, various machine learning (ML) algorithms such as principal component analysis (PCA), k-nearest neighbor (KNN), and support vector machine (SVM) have been applied to the development of e-nose systems. However, most studies used the sensor's steady-state response, such as the relative resistance change value at the end of the gas reaction, as the training data. Therefore, it is necessary to wait until the redox reactions between the metal oxide and the gases are completed, and real-time gas prediction is impossible. Also, it is difficult to distinguish gases with similar gas response. In this study, a CNN algorithm was chosen for the development of a real-time selective gas prediction system. Using CNN, which is a kind of supervised learning, pattern recognition was conducted on two-dimensional (x-axis, time; y-axis, sensor signal) data of sensor responses that change differently depending on each target gas. This comparison is also depicted in Figure S13 (Supporting Information). Before training the CNN model, preprocessing was performed on the gas test data collected from the multi-μLED gas sensors in the previous section. To increase the accuracy of the CNN model, more data sets are required for training, and thus both experimentally measured and artificially made data were used for CNN training. In the same gas experiment, there was a difference in gas response (R_{gas}/R_0) within 10% (Figure 3b), so ±10% deviation was applied to the sensor signal (R_{gas}) in the response and recovery section to generate the artificial data. In summary, after repeating the same experiment twice, a total of 6 cycles of gas test data were used, including original and artificially made data: cycles $1^{original}$, $1^{+10\%}$, $1^{-10\%}$, $2^{original}$, $2^{+10\%}$, $2^{-10\%}$ (Figure S14, Supporting Information). To prevent the CNN model from being trained by focusing only on highly reactive gases such as NO_2, normalization was performed by $\log_{10}$, and $\log_{10}(R/R_0)$ was used for the training data. Next, data obtained by sensors 1 and 2 were concatenated in the form of a 2 (number of sensors) × time (s) matrix, and the sampling rate was 1 Hz. A unique transient sensor signal generated by each target gas was captured by a sliding time window of size 2 × 30 (s). The selective gas prediction performance of the CNN model according to the size of the sliding time window will be described in a later section. When training the CNN model, the preprocessed gas response data and the corresponding true label (gas type and concentration) were put together. In the classification of gas types, air, ethanol, NO_2, acetone, and methanol gases were labeled as 0, 1, 2, 3, and 4, respectively. In the regression of gas concentration, normalization was
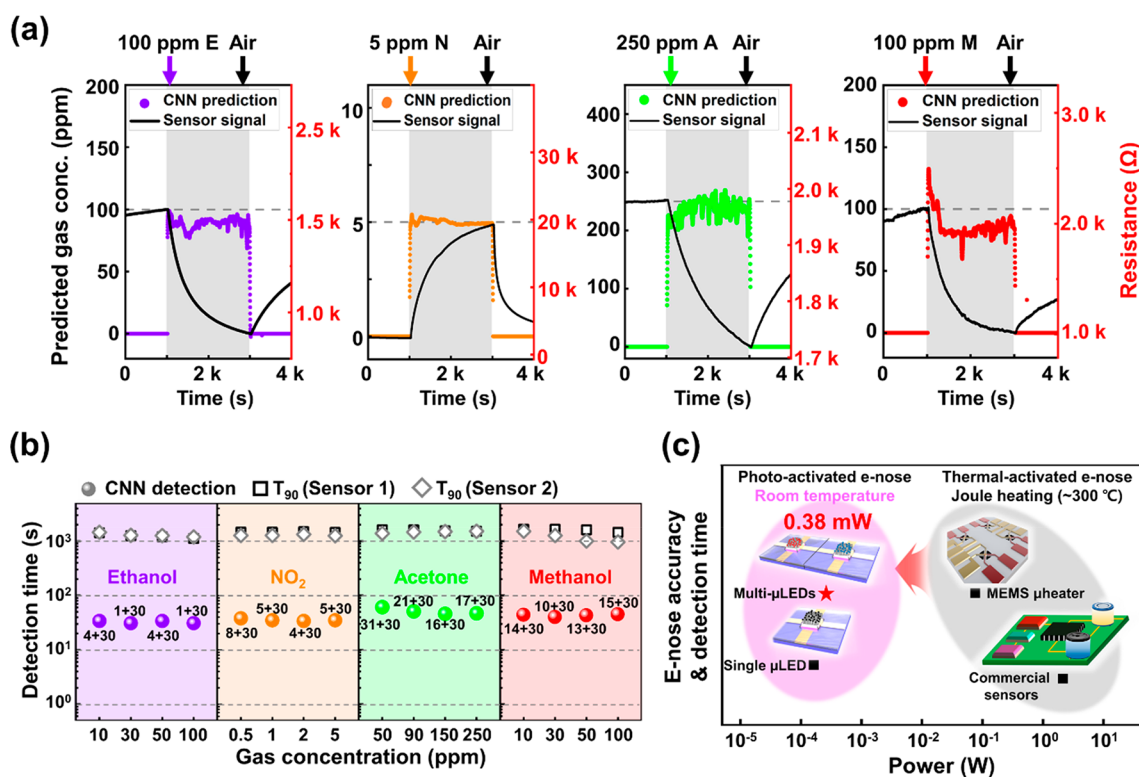
Figure 5. Advantages of the e-nose system based on multi-μLEDs and CNN algorithm. (a) Graph comparing real-time sensor signal for 100 ppm ethanol (E), 5 ppm NO$_2$ (N), 250 ppm acetone (A), and 100 ppm methanol (M), and CNN model prediction results. The black line in the graph represents the real-time sensor signal of sensor 2 (GLAD In$_2$O$_3$ coated with Au NPs). (b) Comparison of detection times between T_{90} of the raw sensor signal and CNN model. (c) Power efficiency of μLED-based e-nose compared to heater-based e-nose system. Total power consumption has been reduced to less than one-hundredth that of a thermally activated e-nose system.

performed by dividing the gas concentration by the maximum concentration of each target gas (0 to 1) since their original values are different for each gas. In the CNN model, six kernels with a size of 2 × 10 s were used as convolution layers, and the stride interval was set to 5 s. After convolution, it led to fully connected (FC) layers of 64, 32, 16, and 8 nodes. In each hidden layer of the CNN and FC, batch-normalization (BN) and leaky-rectified linear unit (leaky-ReLU) activation function was used. The final output layer has 6 nodes, of which 5 were used for gas type classification and the other node was used for the regression of gas concentration. The classification was performed by softmax function and the 5 classification nodes output the gas labels with the highest probability. The regression node outputs normalized predicted gas concentration values through regression analysis. The classification and regression loss functions used in this study were the categorical cross-entropy, $L_{\text{cross-entropy}}$ and mean-squared error, L_{MSE}, respectively. Since the CNN model performs classification and regression simultaneously, the total loss function was defined as $L_{\text{total}} = w \cdot L_{\text{cross-entropy}} + (1 - w) \cdot L_{\text{MSE}}$ (w = weight). During CNN model training, an Adam optimizer with a learning rate, $\eta = 10^{-4}$ was used to minimize the L_{total}, and after several hyperparameter tuning processes, w of 0.05 and epochs of 1000 showed the best prediction results. The results were obtained by forward-propagation of one cycle amount of gas test data set into the trained CNN model that was not used for training. Finally, the outputs of the CNN model were filtered during postprocessing to reduce noise. When the CNN model predicted the air condition, the regression prediction value was set to 0, and after that, a mode filter was used for classification and an average filter was used for regression.

The results of the e-nose system based on multi-μLED gas sensors and CNN are shown in Figure 4b,cd. Gas type classification results for five different gases (air, ethanol, NO$_2$, acetone, and methanol) are summarized in the confusion matrix (Figure 4b). The total accuracy of classification was 99.32%. Figure 4c shows the gas concentration regression results at normalized gas concentration (0−1), and the average of the mean absolute error (MAE) was 13.82%. Figure 4d shows the real-time prediction results of each target gas. The classification accuracy is calculated by dividing the number of correct predictions by the total number of data. For each target gas sensing experiment, the classification accuracy was greater than 99% for ethanol, NO$_2$, and acetone and about 95% for methanol gas. The reason that methanol gas has slightly lower accuracy than the other gases is presumed to be due to sensor signal drift for methanol gas. The performance of the e-nose system using only a single sensor was also analyzed. When only sensor 1 (GLAD In$_2$O$_3$ coated with Ag NPs) was used, the classification accuracy was 90.00% and the MAE of the regression was 40.63% (Figure S15, Supporting Information). When only sensor 2 (GLAD In$_2$O$_3$ coated with Au NPs) was used, the classification accuracy was 98.64% and the MAE of the regression was 22.20% (Figure S16, Supporting Information). Especially, the prediction error for methanol gas was considerably larger when a single sensor was used. It was confirmed that the multi-μLED-based e-nose system made of different gas sensing materials had higher gas prediction accuracy than the single μLED-based e-nose system.
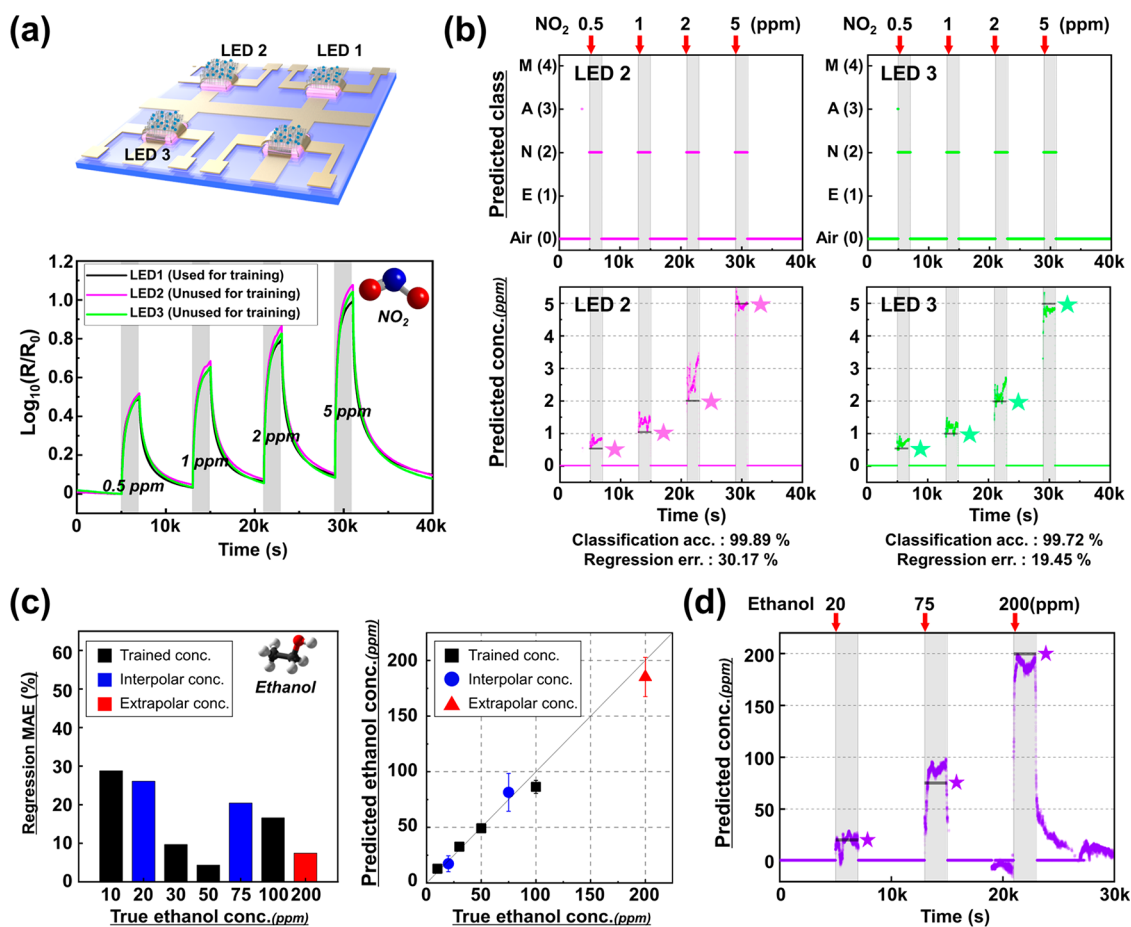
Figure 6. (a) Uniformity of gas response to NO_2 gas between different sensors (LED 1, 2, 3) on the same sensor chip. Response of LED 1 to NO_2 gas was used for the CNN model training, and responses of LEDs 2 and 3 were not used. (b) Real-time prediction results (classification and regression) of LEDs 2 and 3. The CNN model was trained by data obtained from LED 1, and test data obtained from LEDs 2 and 3 were forward-propagated to the CNN algorithm. (c) Prediction results of the untrained gas concentrations (black, trained concentrations; blue, interpolar concentrations; red, extrapolar concentration). (d) Real-time prediction results (regression) of ethanol gas with untrained concentrations.

The monolithic μLED gas sensor has the great advantage of ultra-low-power but has much slower response and recovery compared to the heating-based sensors.[18,19] However, this problem could be resolved by applying the deep learning algorithm. In Figure 5a, the real-time sensor signal is shown as a black line, and the CNN prediction result is shown as a colored dot. It takes more than a thousand seconds for the sensor signal to saturate, but the CNN model can distinguish gases in seconds. The effect of CNN on reducing detection time is clear when comparing the response time, T_{90} (time required for a sensor to reach 90% of the final sensor signal value) with the CNN prediction time. In Figure 5b, the response times T_{90} of sensor 1 and sensor 2 for each target gas are indicated by black squares and gray diamonds, respectively. For practical use, the length of the time window used for preprocessing (30 s) should be added to the CNN prediction time, and it is displayed on the figure. Excluding the size of the time window, ethanol and NO_2 can be detected within 10 s and acetone and methanol within 30 s. A smaller time window size reduces the total time required for prediction but also provides poorer accuracy. On the contrary, a bigger time window size improves accuracy by performing supervised learning with more information from the transient sensor signal but increases the possibility of overfitting and the time

required for prediction. In the Supporting Information, Figure S17 compares the performance of e-nose systems with sliding time window sizes of 10, 15, 20, 30, and 120 s. In situations where rapid gas prediction is required, such as toxic or explosive gases, a smaller time window is recommended. If accurate gas prediction is required, a large time window can be used. As such, the size of the sliding time window can be determined by the target applications. In summary, the multi-μLED gas sensor-based e-nose system has the advantage of ultra-low-power of 0.38 mW, which is less than one-hundredth the power consumption of the heater-based e-nose system (Figure 5c). The slow response and recovery of the μLED gas sensor could be overcome by pattern recognition using a CNN.

Additionally, the uniformity between μLED gas sensors was analyzed. GLAD In_2O_3 coated with Au NPs (same conditions with sensor 2) was deposited on the sensor array on the same sensor chip. In Figure 6a, the NO_2 gas test was conducted simultaneously using a μLED sensor array (LED 1, LED 2, LED 3), and the responses were similar between different sensors. Next, it was tested whether a single CNN model could be shared among different μLED sensors. The data obtained from LED 1 was used as a training data for the CNN model, and the data acquired from LEDs 2 and 3 were not used for

Table 1. Comparison of Heater-Based E-Nose and Photoactivation-Based E-Nose Systems[a]

	thermal activation				photoactivation	
	ref 42	ref 43	ref 44	ref 30	ref 45	this work
sensing materials	ZnO	SnO$_2$	ZnO	MOXs and Au NP coated MOXs	metal/MOX functionalized GaN NWs	**Au, Ag NP coated In$_2$O$_3$**
number of sensors	5	1	1	8	8	**2**
number of target gases	6	4	3	6	6	**5**
total sensor power	ceramic heater (NC)	ceramic heater (NC)	bulk heater (NC)	microheater (88 mW)	365 nm external LED (470 mW/cm^2)	**395 nm monolithic μLEDs (0.38 mW)**
analysis method	SVM (classification) ELM (regression)	RF (classification) MLP (regression)	RF	CNN	SVM	**CNN**
classification accuracy (%)	99.0	85.93	99.8	98.1	100	**99.32**
regression error	R^2 = 0.98	7.13% (MAE)	NC	10.15% (MAE)	NC	**13.82% (MAE)**
real-time prediction	X	X	X	O	X	**O**

[a]MOX, metal oxide; NW, nanowire; NC, not considered; SVM, support vector machine; ELM, extreme learning machine; RF, random forest; MLP, multilayer perceptron; MAE, mean absolute error.

training but were used as test data. The data preprocessing method and CNN model were the same as those previously trained in Figure S16. Figure 6b shows the real-time classification and regression results of LEDs 2 and 3. Although the LEDs 2 and 3 were not used for CNN training, the classification of NO$_2$ and air was possible with an accuracy over 99%. The errors of the concentration prediction of LEDs 2 and 3 were relatively larger than that of LED 1. Also, the prediction of untrained gas concentration via CNN algorithm was conducted. This time, the CNN model was trained only with sensor responses to ethanol gas of 10, 30, 50, and 100 ppm, and predictions were made for untrained concentrations (20, 75, and 200 ppm). To increase the accuracy of concentration prediction, the structure of the CNN model was modified: size of the time window in preprocessing 120 s, number of filters 6, size of the filters 2 × 30 s, stride 10, and epochs 300. In Figure 6c, the gas concentrations used in CNN training are shown in black, the concentration outside the training data range is shown in red (extrapolation), and the concentrations inside the training data range are shown in blue (interpolation). The regression error of the concentrations used for training was generally smaller than that of the untrained concentrations, but the possibility of interpolation and extrapolation was confirmed. Figure 6d shows the real-time prediction results of ethanol gas with untrained concentrations, 20, 75, and 200 ppm.

CONCLUSIONS

In this study, an ultra-low-power e-nose system based on a monolithic UV μLED (λ_{peak} = 395 nm) gas sensor was developed. The distance between the gas sensing material (GLAD In$_2$O$_3$) and the μLEDs was only 1 μm, and thus light energy loss was minimized. The LSPR phenomenon was utilized by coating plasmonic noble metal NPs on porous GLAD In$_2$O$_3$ by e-beam evaporation to maximize the gas response. As a result, 5 ppm NO$_2$ gas can be detected in the 1 μW range with gas responses of 5.2, 253.2, and 571.6 (R_{gas}/R_0) for bare In$_2$O$_3$, Ag NP coated In$_2$O$_3$, and Au NP coated In$_2$O$_3$, respectively. Next, based on two μLED gas sensors with different sensing materials (Ag and Au NP coated In$_2$O$_3$) and the CNN algorithm, an e-nose system capable of selectively discriminating gas types (classification) and predicting gas concentrations (regression) of five different gases (air, ethanol, NO$_2$, acetone, and methanol) was developed. As a result, gas prediction of classification with 99.32% accuracy and

regression with a mean absolute error of 13.82% was possible in real-time. Especially, total power consumption of the μLED-based e-nose system was only 0.38 mW, which is less than one-hundredth of that of the heater-based e-nose system. In Table 1, the μLED-based e-nose system developed in this study is compared with some recent ML algorithm-based e-nose technologies. There are several studies related to e-nose systems that selectively classify gas types and predict the concentration using SMO-type gas sensor and ML algorithms, but a bulk heater was used and the power consumption was high.[42−44] Although the power consumption was reduced by using a microheater, the power consumption was still more than 100 times greater than that of the μLEDs.[30] There was a study using a photoactivated gas sensor to develop an e-nose system, but because an external LED was used, the power consumption was greater than that of the microheaters.[45] The μLED-based e-nose system can be used for a long time even in a battery-powered situation, and it is expected to be highly useful as a mobile sensor in combination with internet of things (IoT) technology. In addition, the μLED-based e-nose system is environmentally friendly because it can be operated at room temperature and its UV emission area is microscale size, so it does not harm human users or the surrounding environment. The proposed technology is expected to be used in the development of next generation ultra-low-power environment IoT systems.

METHODS

Fabrication of UV μLED Gas Sensors. A schematic illustration of the entire fabrication process is shown in Figure S1 (Supporting Information). Most of the fabrication process is similar to our previous work.[21] A 6 μm thick n-GaN, a 50 nm thick InGaN/GaN multi-quantum-well (MQW) activation layer, and a 300 nm thick p-GaN layer were epitaxially grown by metal−organic chemical vapor deposition (MOCVD) on a 600 μm thick patterned sapphire substrate (PSS) (Outsourcing, Soft-epi, Korea). Inductively coupled plasma-reactive ion etching (ICP-RIE) was used to vertically etch the GaN layer and form a 50 × 50 μm^2 mesa structure. An indium tin oxide (ITO) current spreading layer was deposited on the GaN layer by e-beam evaporation, followed by a rapid thermal annealing (RTA) process to increase transparency and electrical conductivity. Gold p and n contact electrodes were patterned by photolithography and e-beam evaporation. For insulation, the first SiO$_2$ layer was deposited by a plasma-enhanced chemical vapor deposition (PECVD) process, and the PECVD SiO$_2$ was etched vertically *via* RIE to open the p and n contact electrodes. Then, the gold contact electrodes were patterned by photolithography and e-beam evaporation. A second SiO$_2$ layer

was deposited by the PECVD process and vertically etched *via* RIE to once again open the p and n contact pads. Gold interdigitated sensor electrodes were patterned on the μLED platform by photolithography and e-beam evaporation. The fabricated μLED gas sensor was diced into a single sensor chip of 5×5 mm^2 through blade dicing (Sapphire dicing blades, Disco, Japan).

Glancing Angle Deposition of Nanocolumnar In$_2$O$_3$ Films and Metal NP Coating. A high purity (99.99%) In$_2$O$_3$ sputtering target was used for GLAD radio frequency (RF) sputtering. Prior to GLAD deposition of In$_2$O$_3$ on the μLED gas sensor platform, polyimide (PI) tape was attached to the electrical contact pads of the μLED to prevent electrical short. The interdigitated sensor electrode areas were exposed from the PI tape protection, and the In$_2$O$_3$ target material could be deposited through the GLAD process. The working conditions of GLAD sputtering are as follows: working pressure 4 mTorr in argon atmosphere, tilt angle of substrate 85°, rotation speed of substrate 3.6 rpm, RF power 250 W, total process time 90 min (30 + 30 + 30 min with 10 min cooling interval). Before coating the metal NPs on the GLAD In$_2$O$_3$ surface, oxygen plasma ashing was conducted at 50 W RF power for 1 min to remove organic residues. Then, Ag and Au NPs were coated on the surface of the nanostructured metal oxide through e-beam evaporation. Their target thicknesses were 2.5 and 2.0 nm, respectively, based on a deposition monitoring quartz crystal microbalance (QCM) sensor, and the deposition rate was 0.1 Å/s.

Optical Characterization of the UV Micro-LEDs and NP Coated GLAD In$_2$O$_3$. The light emission spectrum and light−current−voltage (L-I-V) properties of the UV μLEDs were obtained using a wafer-level LED measurement system (OPI-160, WITH-LIGHT, Korea) equipped with an integrating sphere and a sourcemeter (Keithley 2400, USA). The absorbance of GLAD In$_2$O$_3$, GLAD In$_2$O$_3$ coated with metal NPs, and the metal NPs themselves were analyzed with an ultraviolet−visible (UV−vis) spectrophotometer (Lambda 1050, PerkinElmer, USA). The afore-mentioned materials were deposited on 1×1 cm^2 transparent quartz substrates for absorbance measurement.

Material Characterizations. The nanostructures of GLAD In$_2$O$_3$ coated with Ag and Au NPs were observed with an ultra-high-resolution field emission-scanning electron microscope (UHR FE-SEM SU8230, Hitachi, Japan). The cross-sectional image and energy dispersive spectrum (EDS) mapping of metal NP coated GLAD In$_2$O$_3$ films were taken by a transmission electron microscope (Tecnai G^2 F30 S-TWIN, FEI, Netherlands) and a dual beam focused ion beam (FIB) system (Helios NanoLab, FEI, Netherlands), respectively. X-ray diffraction (XRD) analysis of the GLAD In$_2$O$_3$ film was conducted by an X-ray diffractometer (SmartLab, RIGAKU, Japan). X-ray photoelectron spectroscopy (XPS) analysis of metal NP coated GLAD In$_2$O$_3$ was conducted using an in situ X-ray photoelectron spectrometer system (Nexsa G2, Thermo Scientific, USA).

Gas Tests. The μLED gas sensor was mounted on a printed circuit board (PCB), and gold wire bonding was conducted. The μLED-mounted PCB was then placed in a custom polycarbonate (PC) enclosure and connected to a dual channel sourcemeter (2636B, Keithley, USA) to forward bias the μLED and simultaneously measure the sensor resistance. An accurate flow rate of dry (0% relative humidity) target gases (ethanol, NO$_2$, acetone, methanol) was controlled by a mass flow controller (AFC500, ATOVAC, Korea), and gases were injected into the PC enclosure (Figure S18, Supporting Information).

Deep-Learning-Based Gas Prediction. A CNN model was constructed using an open source machine learning library (PyTorch, Meta, USA). The training of the CNN model and analysis of the results were conducted using a high-performance GPU (RTX Titan, NVIDIA, USA) based computing environment.

ASSOCIATED CONTENT

Ⓢ Supporting Information

The Supporting Information is available free of charge at https://pubs.acs.org/doi/10.1021/acsnano.2c09314.

Additional explanation of μLED gas sensors (Fabrication process, improvements in the sensor design compared to the previous study), characterization of μLED gas sensors (L−I−V properties, optical microscope images, gas test results), material analysis results (SEM images of porous GLAD In$_2$O$_3$ film, image J particle analysis), and the results of a study using CNN not included in the manuscript (PDF)

AUTHOR INFORMATION

Corresponding Authors

Kuk-Jin Yoon − *Department of Mechanical Engineering, Korea Advanced Institute of Science and Technology (KAIST), Daejeon 34141, Republic of Korea*; Email: kjyoon@kaist.ac.kr

Yong-Hoon Cho − *Department of Physics and KAIST Institute for the NanoCentury, Korea Advanced Institute of Science and Technology (KAIST), Daejeon 34141, Republic of Korea*; Email: yhc@kaist.ac.kr

Inkyu Park − *Department of Mechanical Engineering, Korea Advanced Institute of Science and Technology (KAIST), Daejeon 34141, Republic of Korea; KAIST Institute for the NanoCentury, Korea Advanced Institute of Science and Technology (KAIST), Daejeon 34141, Republic of Korea;* ⓘ orcid.org/0000-0001-5761-7739; Email: inkyu@kaist.ac.kr

Authors

Kichul Lee − *Department of Mechanical Engineering, Korea Advanced Institute of Science and Technology (KAIST), Daejeon 34141, Republic of Korea*

Incheol Cho − *Department of Mechanical Engineering, Korea Advanced Institute of Science and Technology (KAIST), Daejeon 34141, Republic of Korea*

Mingu Kang − *Department of Mechanical Engineering, Korea Advanced Institute of Science and Technology (KAIST), Daejeon 34141, Republic of Korea*

Jaeseok Jeong − *Department of Mechanical Engineering, Korea Advanced Institute of Science and Technology (KAIST), Daejeon 34141, Republic of Korea*

Minho Choi − *Department of Physics, Korea Advanced Institute of Science and Technology (KAIST), Daejeon 34141, Republic of Korea*

Kie Young Woo − *Department of Physics, Korea Advanced Institute of Science and Technology (KAIST), Daejeon 34141, Republic of Korea*

Complete contact information is available at:
https://pubs.acs.org/10.1021/acsnano.2c09314

Author Contributions

The manuscript was written through contributions of all authors. K. Lee conducted all experiments, analyzed the data, and wrote the paper. I. Cho and J. Jeong discussed the development of the machine learning algorithm. M. Kang, M. Choi, and K. Woo discussed the fabrication of the μLED gas sensors. K. Yoon, Y. Cho, and I. Park supervised the project. All authors have given approval to the final version of the manuscript.

Notes

The authors declare no competing financial interest.

REFERENCES

(1) Vohra, K.; Vodonos, A.; Schwartz, J.; Marais, E. A.; Sulprizio, M. P.; Mickley, L. J. Global Mortality from Outdoor Fine Particle Pollution Generated by Fossil Fuel Combustion: Results from GEOS-Chem. *Environ. Res.* **2021**, *195*, 110754.

(2) Bany Salameh, H. A.; Dhainat, M. F.; Benkhelifa, E. An End-to-End Early Warning System Based on Wireless Sensor Network for Gas Leakage Detection in Industrial Facilities. *IEEE Syst. J.* **2021**, *15*, 5135−5143.

(3) Mendes, L. B.; Ogink, N. W. M.; Edouard, N.; van Dooren, H. J. C.; Tinôco, I. de F. F.; Mosquera, J. NDIR Gas Sensor for Spatial Monitoring of Carbon Dioxide Concentrations in Naturally Ventilated Livestock Buildings. *Sensors* **2015**, *15*, 11239−11257.

(4) Love, C.; Nazemi, H.; El-Masri, E.; Ambrose, K.; Freund, M. S.; Emadi, A. A Review on Advanced Sensing Materials for Agricultural Gas Sensors. *Sensors* **2021**, *21*, 3423.

(5) Ortiz Perez, A.; Bierer, B.; Scholz, L.; Wollenstein, J.; Palzer, S. A Wireless Gas Sensor Network to Monitor Indoor Environmental Quality in Schools. *Sensors* **2018**, *18*, 4345.

(6) Liu, W.; Xu, L.; Sheng, K.; Zhou, X.; Dong, B.; Lu, G.; Song, H. A Highly Sensitive and Moisture-Resistant Gas Sensor for Diabetes Diagnosis with Pt@In_2O_3 Nanowires and a Molecular Sieve for Protection. *NPG Asia Mater.* **2018**, *10*, 293−308.

(7) Yuan, Z.; Bariya, M.; Fahad, H. M.; Wu, J.; Han, R.; Gupta, N.; Javey, A. Trace-level, Multi-Gas Detection for Food Quality Assessment Based on Decorated Silicon Transistor Arrays. *Adv. Mater.* **2020**, *32*, 1908385.

(8) Liu, F.; Zhang, Y.; Yu, Y.; Xu, J.; Sun, J.; Lu, G. Enhanced Sensing Performance of Catalytic Combustion Methane Sensor by Using Pd Nanorod/γ-Al_2O_3. *Sens. Actuators, B* **2011**, *160*, 1091−1097.

(9) Del Orbe Henriquez, D.; Cho, I.; Yang, H.; Choi, J.; Kang, M.; Chang, K. S.; Jeong, C. B.; Han, S. W.; Park, I. Pt Nanostructures Fabricated by Local Hydrothermal Synthesis for Low-Power Catalytic-Combustion Hydrogen Sensors. *ACS Appl. Nano Mater.* **2021**, *4*, 7−12.

(10) Wan, H.; Yin, H.; Lin, L.; Zeng, X.; Mason, A. J. Miniaturized Planar Room Temperature Ionic Liquid Electrochemical Gas Sensor for Rapid Multiple Gas Pollutants Monitoring. *Sens. Actuators, B* **2018**, *255*, 638−646.

(11) Wan, H.; Gan, Y.; Sun, J.; Liang, T.; Zhou, S.; Wang, P. High Sensitive Reduced Graphene Oxide-Based Room Temperature Ionic Liquid Electrochemical Gas Sensor with Carbon-Gold Nano-composites Amplification. *Sens. Actuators, B* **2019**, *299*, 126952.

(12) Dinh, T. V.; Choi, I. Y.; Son, Y. S.; Kim, J. C. A Review on Non-Dispersive Infrared Gas Sensors: Improvement of Sensor Detection Limit and Interference Correction. *Sens. Actuators, B* **2016**, *231*, 529−538.

(13) Dey, A. Semiconductor Metal Oxide Gas Sensors: A Review. *Mater. Sci. Eng., B* **2018**, *229*, 206−217.

(14) Long, H.; Turner, S.; Yan, A.; Xu, H.; Jang, M.; Carraro, C.; Maboudian, R.; Zettl, A. Plasma Assisted Formation of 3D Highly Porous Nanostructured Metal Oxide Network on Microheater Platform for Low Power Gas Sensing. *Sens. Actuators, B* **2019**, *301*, 127067.

(15) Xie, D.; Chen, D.; Peng, S.; Yang, Y.; Xu, L.; Wu, F. A Low Power Cantilever-Based Metal Oxide Semiconductor Gas Sensor. *IEEE Electron Device Lett.* **2019**, *40*, 1178−1181.

(16) Lim, Y.; Lee, S.; Kwon, Y. M.; Baik, J. M.; Shin, H. Gas Sensor Based on a Metal Oxide Nanowire Forest Built on a Suspended Carbon Nano-Heater. *IEEE Micro Electro Mech. Syst.* **2018**, 905−907.

(17) Meng, G.; Zhuge, F.; Nagashima, K.; Nakao, A.; Kanai, M.; He, Y.; Boudot, M.; Takahashi, T.; Uchida, K.; Yanagida, T. Nanoscale Thermal Management of Single SnO_2 Nanowire: Pico-Joule Energy Consumed Molecule Sensor. *ACS Sens.* **2016**, *1*, 997−1002.

(18) Suh, J. M.; Eom, T. H.; Cho, S. H.; Kim, T.; Jang, H. W. Light-Activated Gas Sensing: a Perspective of Integration with Micro-LEDs and Plasmonic Nanoparticles. *Mater. Adv.* **2021**, *2*, 827−844.

(19) Kumar, R.; Liu, X.; Zhang, J.; Kumar, M. Room-Temperature Gas Sensors under Photoactivation: From metal oxides to 2D materials. *Nano-Micro Lett.* **2020**, *12*, 164.

(20) Jaisutti, R.; Kim, J.; Park, S. K.; Kim, Y. H. Low-Temperature Photochemically Activated Amorphous Indium-Gallium-Zinc Oxide for Highly Stable Room-Temperature Gas Sensors. *ACS Appl. Mater. Interfaces* **2016**, *8*, 20192−20199.

(21) Cho, I.; Sim, Y. C.; Cho, M.; Cho, Y. H.; Park, I. Monolithic Micro Light-Emitting Diode/Metal Oxide Nanowire Gas Sensor with Microwatt-Level Power Consumption. *ACS Sens.* **2020**, *5*, 563−570.

(22) Ponzoni, A.; Baratto, C.; Cattabiani, N.; Falasconi, M.; Galstyan, V.; Nunez-Carmona, E.; Rigoni, F.; Sberveglieri, V.; Zambotti, G.; Zappa, D. Metal Oxide Gas Sensors, a Survey of Selectivity Issues Addressed at the SENSOR Lab, Brescia (Italy). *Sensors* **2017**, *17*, 714.

(23) Hu, W.; Wan, L.; Jian, Y.; Ren, C.; Jin, K.; Su, X.; Bai, X.; Haick, H.; Yao, M.; Wu, W. Electronic Noses: From Advanced Materials to Sensors Aided with Data Processing. *Adv. Mater. Technol.* **2018**, *4*, 1800488.

(24) Liu, H.; Yu, D.; Gu, Y. Classification and Evaluation of Quality Grades of Organic Green Teas Using an Electronic Nose Based on Machine Learning Algorithms. *IEEE Access* **2019**, *7*, 172965−172973.

(25) Chen, H.; Huo, D.; Zhang, J. Gas Recognition in E-Nose System: A review. *IEEE Trans. Biomed. Circuits Syst.* **2022**, *16*, 169−184.

(26) Kang, H.; Cho, S. Y.; Ryu, J.; Choi, J.; Ahn, H.; Joo, H.; Jung, H. T. Multiarray Nanopattern Electronic Nose (E-nose) by High-Resolution Top-Down Nanolithography. *Adv. Funct. Mater.* **2020**, *30*, 2002486.

(27) Chao, S. H.; Yeh, L. H.; Wu, R. T.; Kawagishi, K.; Hsu, S. C. Novel Patterned Sapphire Substrates for Enhancing the Efficiency of GaN-Based Light-Emitting Diodes. *RSC Adv.* **2020**, *10*, 16284.

(28) Wongchoosuk, C.; Wisitsoraat, A.; Phokharatkul, D.; Horprathum, M.; Tuantranont, A.; Kerdcharoen, T. Carbon Doped Tungsten Oxide Nanorods NO_2 Sensor Prepared by Glancing Angle RF Sputtering. *Sens. Actuators, B* **2013**, *181*, 388−394.

(29) Yoon, M.; Lee, S.; Lee, D.; Kim, J.; Moon, J. All-Solid-State Thin Film Battery Based on Well-Aligned Slanted $LiCoO_2$ Nanowires Fabricated by Glancing Angle Deposition. *Appl. Surf. Sci.* **2017**, *412*, 537−544.

(30) Kang, M.; Cho, I.; Park, J.; Jeong, J.; Lee, K.; Lee, B.; Del Orbe Henriquez, D.; Yoon, K.; Park, I. High Accuracy Real-Time Multi-Gas Identification by a Batch-Uniform Gas Sensor Array and Deep Learning Algorithm. *ACS Sens.* **2022**, *7*, 430−440.

(31) Qomaruddin; Casals, O.; Wasisto, H. S.; Waag, A.; Prades, J. D.; Fàbrega, C. Visible-Light-Driven Room Temperature NO_2 Gas Sensor Based on Localized Surface Plasmon Resonance: The Case of Gold Nanoparticle Decorated Zinc Oxide Nanorods (ZnO NRs). *Chemosensors* **2022**, *10*, 28.

(32) Tian, X.; Yang, X.; Yang, F.; Qi, T. A Visible-Light Activated Gas Sensor Based on Perylenediimide-Sensitized SnO_2 for NO_2 Detection at Room Temperature. *Colloids Surf., A* **2019**, *578*, 123621.

(33) Clavero, C. Plasmon-Induced Hot-Electron Generation at Nanoparticle/Metal-Oxide Interfaces for Photovoltaic and Photocatalytic Devices. *Nat. Photonics* **2014**, *8*, 95−103.

(34) Ma, X. C.; Dai, Y.; Yu, L.; Huang, B. B. Energy Transfer in Plasmonic Photocatalytic Composites. *Light: Sci. Appl.* **2016**, *5*, No. e16017.

(35) Mayer, K. M.; Hafner, J. H. Localized Surface Plasmon Resonance Sensors. *Chem. Rev.* **2011**, *111*, 3828−3857.

(36) Wang, C.; Astruc, D. Nanogold Plasmonic Photocatalysis for Organic Synthesis and Clean Energy Conversion. *Chem. Soc. Rev.* **2014**, *43*, 7188−7216.

(37) Wang, X. X.; Zhang, S.; Liu, Y.; Dai, J. N.; Li, H. Y.; Guo, X. Light-Excited Chemiresistive Sensors Integrated on LED Microchips. *J. Mater. Chem. A* **2021**, *9*, 16545−16553.

(38) Gall, D. Electron Mean Free Path in Elemental Metals. *J. Appl. Phys.* **2016**, *119*, 085101.

(39) Prades, J. D.; Jimenez-Diaz, R.; Manzanares, M.; Hernandez-Ramirez, F.; Cirera, A.; Romano-Rodriguez, A.; Mathur, S.; Morante, J. R. A Model for the Response Towards Oxidizing Gases of Photoactivated Sensors Based on Individual SnO_2 Nanowires. *Phys. Chem. Chem. Phys.* **2009**, *11*, 10881−10889.

(40) Alenezi, M. R.; Alshammari, A. S.; Jayawardena, K. D. G. I.; Beliatis, M. J.; Henley, S. J.; Silva, S. R. P. Role of the Exposed Polar Facets in the Performance of Thermally and UV Activated ZnO Nanostructured Gas Sensors. *J. Phys. Chem. C* **2013**, *117*, 17850−17858.

(41) Chinh, N. D.; Quang, N. D.; Lee, H.; Thi Hien, T.; Hieu, N. M.; Kim, D.; Kim, C.; Kim, D. NO Gas Sensing Kinetics at Room Temperature under UV Light Irradiation of In_2O_3 Nanostructures. *Sci. Rep.* **2016**, *6*, 35066.

(42) Wang, T.; Ma, H.; Jiang, W.; Zhang, H.; Zeng, M.; Yang, J.; Wang, X.; Liu, K.; Huang, R.; Yang, Z. Type Discrimination and Concentration Prediction towards Ethanol Using a Machine Learning-Enhanced Gas Sensor Array with Different Morphology-Tuning Characteristics. *Phys. Chem. Chem. Phys.* **2021**, *23*, 23933.

(43) Acharyya, S.; Jana, B.; Nag, S.; Saha, G.; Guha, P. K. Single Resistive Sensor for Selective Detection of Multiple VOCs Employing SnO_2 Hollowspheres and Machine Learning Algorithm: A Proof of Concept. *Sens. Actuators, B* **2020**, *321*, 128484.

(44) Kanaparthi, S.; Singh, S. G. Discrimination of Gases with a Single Chemiresistive Multi-Gas Sensor Using Temperature Sweeping and Machine Learning. *Sens. Actuators, B* **2021**, *348*, 130725.

(45) Khan, M. A. H.; Thomson, B.; Debnath, R.; Motayed, A.; Rao, M. V. Nanowire-Based Sensor Array for Detection of Cross-Sensitive Gases Using PCA and Machine Learning Algorithms. *IEEE Sens. J.* **2020**, *20*, 6020.

▥ Recommended by ACS